IOP Publishing Superconductor Science and Technology
Supercond. Sci. Technol. 33 (2020) 035004 (7pp) https://doi.org/10.1088/1361-6668/ab6ec5

Dominant factors for the pinning enhancement by large artificial partial and complete antidots in superconducting films

A Jones[1,2], M Al-Qurainy[1], A Hamood[1], S K H Lam[2] and A V Pan[1,3]

[1] Institute for Superconducting and Electronic Materials, University of Wollongong, Northfields Avenue, Wollongong, NSW 2522, Australia
[2] CSIRO Manufacturing, Bradfield Road, West Lindfield, 2070 NSW, Australia
[3] National Research Nuclear University MEPhI (Moscow Engineering Physics Institute), 31 Kashirskoye Shosse, 115409, Moscow, Russia

E-mail: pan@uow.edu.au

Received 7 November 2019, revised 24 December 2019
Accepted for publication 22 January 2020
Published 4 February 2020

Abstract

Partially (blind) or fully perforated antidots (BADs or ADs, respectively) fabricated by laser lithography and ion beam etching in superconducting $YBa_2Cu_3O_7$ (YBCO) films possess a cumulative circumference wall surface, which is found to be responsible for pinning vortices and/or magnetic flux, whereby increasing the critical current density (J_c) relative to corresponding plain (unpatterned) films. Using a variety of contrastingly shaped, relatively large 2–5 μm BADs and ADs, the J_c of YBCO thin films has been effectively increased within the relatively narrow band of wall surfaces of antidots, independent whether patterns are AD or BAD type. Independence of antidot types indicates that enhancement is insensitive whether magnetic flux is inside the ADs, or vortices are inside the BADs. Within this AD wall surface band region a clear shape dependence also emerges. This finding may also provide a guide for superconducting devices requiring maximal J_c and reduced associated vortex movement noise.

Keywords: antidot, critical current density, flux pinning, defect wall, YBCO thin films

(Some figures may appear in colour only in the online journal)

1. Introduction

Improving, modifying and controlling the critical current density (J_c) of superconductors is necessary for existing and potential devices. Tailored flux pinning in $YBa_2Cu_3O_7$ (YBCO) using artificial and natural defects can provide the necessary J_c enhancements. Major studies in film microstructure alterations such as multilayering [1, 2], addition of secondary phase nanocomposites [3–6], nanorods [7–9] or ion irradiation [10–12] have proved successful.

Lithographic nanofabrication techniques by the complete or partial removal of the superconductor provide vortex and/or flux trapping in small and controlled locations [13–22], which allows more regulated and, possibly, complementary vortex manipulation and guidance. The so-named antidots (ADs) provide areas of reduced, or zero, superconducting potential and may be specifically designed to match vortex lattices, further increasing the energy required to move the vortices. Due to the flux pinning capabilities of the ADs, generally their use has been in both reduction of vortex movement and its associated noise [23–25] and enhancement of J_c [15, 18].

Progress with this type of defect has been limited by the size of the AD, which has generally been around tens to hundreds of nanometers with one reason being that ADs could accommodate only one or a few vortices. This limits J_c and vortex control to only tiny applied magnetic field (B_a) range, mainly around the so-called single vortex pining regime. Another problem lies with the difficulty of producing AD on such a scale, in both time and expenditure, in particularly on an industrial scale [26]. One obvious way to fix this would be to increase the size of the AD. In doing so optical laser lithography (with μm resolution) can be used rather than electron beam lithography (with nm resolution). However, the

most important aspect of this size increase is to ensure the J_c is reliably and controllably increased. Defects this large have been shown to increase the J_c of YBCO thin films. This includes both modifying the location of the ADs to a graded or non-uniform landscape [15] and by reducing the size of the hole to 2 μm to around the resolution limit of laser lithography [18]. Another application of micron sized holes is the ability to create a ratchet effect [19, 27].

In this work, micron-sized defects much larger than the magnetic field penetration depth (λ) provide the pinning landscape such that the J_c enhancement can be investigated, so that some generalization of such behavior can be drawn. We have found that partially (or blind BADs) or fully perforated antidots (ADs) fabricated by laser lithography and ion etching in YBCO films produce a consistent J_c enhancement if the circumference wall of antidots has the rather narrow optimal surface area, which is independent of shape and type of antidots.

2. Experimental details

YBCO thin films of ~250 nm thickness have been grown on 5 × 5 mm^2 $LaAlO_3$ (LAO) substrates by our well-established PLD process, which is described elsewhere [1, 28, 29]. Their critical temperature and critical current density are typically $T_c = (91.5 \pm 0.5)$ K and $J_c \simeq 3.5 \times 10^{10}$ Am^{-2} at 77 K, respectively showing consistent high quality.

Laser lithography (Heidelberg Instruments μPG 101) and ion beam etching (IBE) were used to define the bridges and patterns [30, 29]. The two families of samples used were created with artificial defects being etched entirely through the YBCO (fully perforated ADs) and etched partially through the YBCO (blind hole ADs denoted as BADs). The shapes and sizes of the artificial defects were the same for both families with the all blind patterns used are shown in figure 1. Note the typical rounded edges for samples BB, SB, TB and T2B are due to the limited resolution of the laser lithography used.

The sizes of the respective defects are defined by the height of the 5 μm boomerangs denoted as B (figure 1(a)); by the diameter of the 2–3 μm circles denoted as C (figure 1(b)), and by the long edge of the pattern for 2–3 μm squares (S) and triangles (T and T2) shown in figures 1(c)–(f), respectively. The nomenclature of the blind hole patterns was defined by an additional B, e.g. circles would be CB. If size is not specified it represents the 3 μm patterns, as these made up the majority of artificial defects investigated. In all bridge samples, a control unetched plain (P) region was also present (figure 1(e)).

Standard equilateral triangle, circle and square shapes were used. For the boomerang shapes, an equilateral triangle is initially defined, with the base removed in a triangle shape as well. The apex of the inside elbow is 40% of the maximum height to give a typical boomerang look. The boomerang shape has been tested with a view to achieve ratcheting effects in the future, and to maximize the circumference of the shape to volume removed. The lattice period was 10 μm in a triangular array for all patterns, except T2 which had a 10 μm horizontal period and a 30 μm vertical spacing in a triangular array.

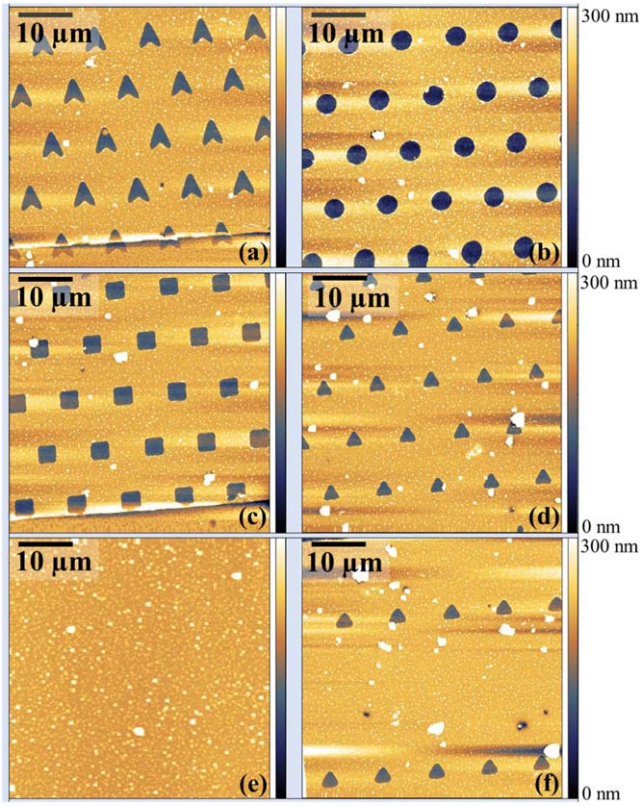

Figure 1. AFM images for blind (a) boomerangs (BB), (b) circles (CB), (c) squares (SB), (d) triangles (TB), (e) plain (P) and (f) triangles 2 (T2B).

The fully perforated AD patterns were etched at the same time as bridge definition to ensure complete removal of YBCO. For the BAD patterns, the bridges were defined first by lithography and IBE, and then the patterns applied on top of the bridge to be etched again. Cross sectional examination of BAD in figure 1 reveals an etch depth of 100 nm for all blind holes, meaning 150 nm of YBCO left within the defect. Patterning of bridges with either blind or fully perforated holes did not change the T_c characteristics. Both sample types were very similar, starting the superconducting transition at (91.5 ± 0.5) K and reaching zero resistance at (88.5 ± 0.5) K.

Resistance measurements were performed in a Quantum Design Magnetic Properties Measurement System . For T_c measurements a current of 10 μA was applied and temperature sweep rate of 2 K min^{-1}. A critical voltage of 10 μV cm^{-1} between contacts was used to determine I_c.

The J_c of each bridge was taken as $I_c/(w_p \times d_p)$, where w_p is the bridge width and d_p the bridge thickness, with the volume removed by the etched defects taken into account. The difference in J_c is given by $\Delta J_c = (J_c^{\text{pattern}} - J_c^{\text{plain}})/J_c^{\text{plain}} \times 100(\%)$.

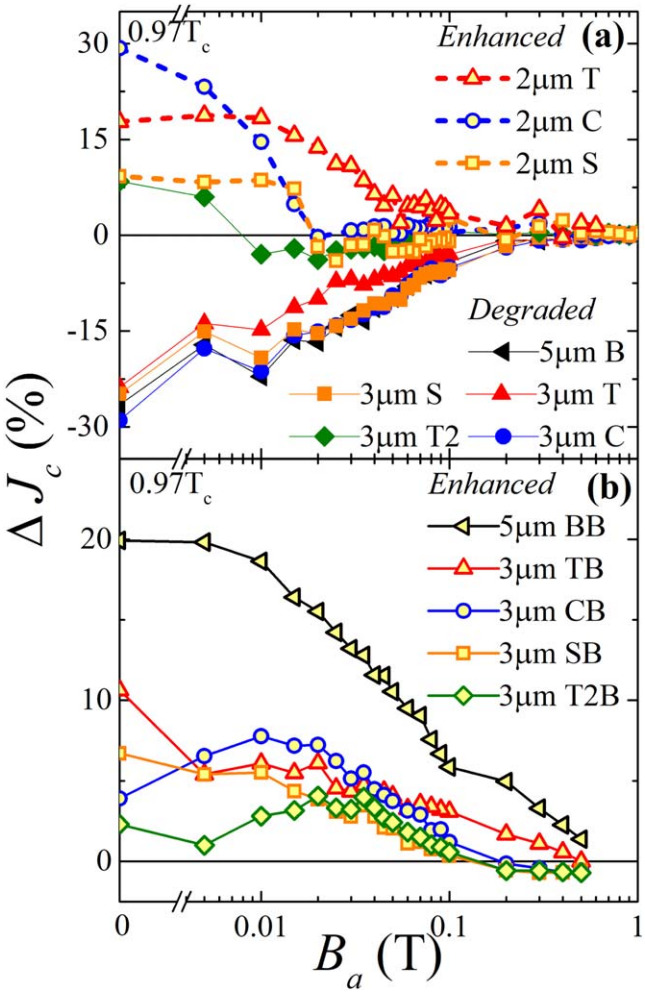

Figure 2. J_c difference calculated by magnetisation measurements at 86 K (0.97 T_c) for (a) fully perforated ADs and (b) blind holes.

3. Results and discussion

3.1. Comparison of fully perforated AD and BAD patterns

A clear ΔJ_c dependence on defect type and shape is observed across all B_a up to 1 T (figure 2). The degradation of J_c caused by the larger (3–5 μm) patterns in figure 2(a) appears to somewhat uniformly follow the amount of volume removed. The highest etched volume for boomerang shaped ADs has caused the most J_c degradation, and T2 the least. Table 1 shows the volume per hole removed for each shape of AD, as well as the total removed volume compared to the volume of the entire film. On the other hand, reducing the volume of the ADs to that of the 2 μm shapes leads to an increased J_c relative to the plain film. This is consistent with the results found in [18], as well as converging to the apparent optimal AD size $\sim\lambda$ [13, 31].

The 2 μm patterns also provide evidence for a pinning potential shape dependence. The 2 μm T sample has less enhancement at lower fields compared to 2 μm C, but the enhancement extends over a much broader B_a, even though the volume removed is much lower for 2 μm T (table 1). The 2 μm S, with the largest volume removed, shows the least J_c increase. Shape/volume dependence is discussed further in the 'Pinning model' section.

Table 1. Volume statistics for all samples measured. Where V_{total} is the total volume removed from etching, $V_{film} = 3750\ \mu m^3$ and D_w is the area of the pinning wall.

Sample	Shape	V_{hole} (μm^3)	V_{total}/V_{film} (%)	D_w (μm^2)
T2B	Triangle	0.46	0.61	0.90
T2	Triangle	1.14	1.52	2.25
TB	Triangle	0.46	1.84	2.90
CB	Circle	0.94	3.76	3.26
SB	Square	0.96	3.84	3.72
2 μmT	Triangle	0.42	1.68	4.50
BB	Boomerang	1.00	4.00	4.93
2 μmC	Circle	1.01	4.05	5.34
2 μmS	Square	1.10	4.40	6.30
T	Triangle	1.14	4.56	7.25
C	Circle	2.35	9.40	8.17
S	Square	2.40	9.60	9.30
B	Boomerang	2.50	10.00	12.30

The J_c enhancement over a broader range of B_a for all the shapes of BADs in figure 2(b) is in direct contrast to that of ADs in figure 2(a). It is also contrary to the behavior of much smaller holes being only a few coherence length (ξ) large [32], for which fully perforated holes were found to be more effective. Surprisingly, the 5 μm BB sample displays the highest magnitude and broadest ΔJ_c enhancement even though the largest volume was removed within the blind sample family. No current rectification was observed in the asymmetrical samples, likely due to the low density of BADs or ADs, the large size of the defects relative to the size of a vortex and the rounded edges in figures 1(a), (d), (f). Similar measurements were also taken at $T = 84$ K ($\simeq$0.95 T_c) for nearly identical results.

3.2. Comparison between shapes of ADs

The difference is taken between ΔJ_c values of the respective BAD and AD shapes, that is, $\Delta J_c^{BAD}(\%)$–$\Delta J_c^{AD}(\%)$ $=\Delta J_c^{difference}(\%)$, and plotted in figure 3. The difference shows how much more effective the respective blind patterns are compared to the AD. The BAD patterns are obviously more effective at increases J_c over the entire field range, with some relatively minor exceptions for T2 type samples, which have had the smallest number of artificial defects introduced and resulted in the smallest ΔJ_c. The higher degree of effectiveness for blind holes is in contrary to the effectiveness of small blind holes (of the order of a few ξ) found in [32].

Figure 3 generally shows three distinct areas of difference, again based on the amount of volume removed. As expected the largest difference in effectiveness is displayed by the B patterns. This is due to fact that it is the most effective blind pattern, and most degraded AD pattern. The likely cause of this is that the largest volume etched from its AD causes the highest level of degradation. On the other hand, the BB provides an effective patterns with the longest additional

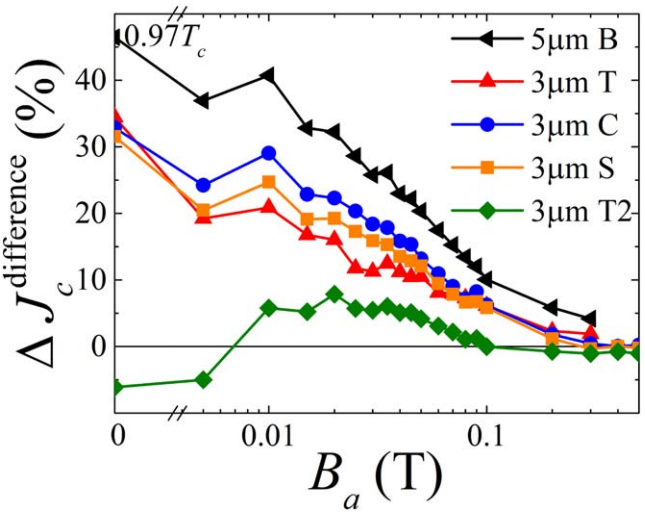

Figure 3. Comparison of J_c differences calculated by magnetisation measurements for 3 μm patterns between fully perforated AD patterns and BAD patterns.

pinning at the walls on the edges of the etched BAD regions [28, 30, 33], while maintaining [34] the inherent vortex pinning natural to PLD YBCO thin films [1, 29, 35] within the BAD regions that are intact and still about ~150 nm thick for all the BAD patterns.

While it would be straightforward to conclude that the J_c enhancement directly depends on the volume of removed superconductor, this is clearly not the case. The C pattern have the second highest ΔJ_c difference, while the third largest volume removed (table 1).

In addition, it appears that the larger the degradation is for AD patterns in figure 2(a), the larger the enhancement is observed for BAD patterns in figure 2(b), which leads to the largest ΔJ_c difference in figure 3. One exception to this dependence appears to be for 3 μm T2, where the AD case is more effective for $B_a < 0.01$ T and $B_a > 0.1$ T, showing that ADs can be better pinning centers than BADs in some cases. This is likely due to the reduced AD density in the T2 case.

General shape of the curve was again similar to that at 0.95 T_c, hence not shown. However, this effectiveness reversal between the defect types occurred at a higher field (possibly due to lower T of these measurements.

3.3. Comparison between magnetic and transport measurements

For a better understanding of the effect large ADs incur onto a YBCO thin film, magnetic (*mag*) and transport (*trans*) have been performed. Indeed, samples with fully perforated AD patters can be expected to respond differently to magnetic measurements [36], which may produce meaningful signals even for granular samples, and to transport measurements, which favor structurally continuous samples with continuous current paths. In addition, while either method may give an accurate value for J_c, certain considerations of electric field criteria used for different types of measurements may be required [37]. Obviously, different electric field criteria used in magnetic and transport measurements assume different degrees of vortex motion involved, generating energy losses [37, 38]. Different vortex motions can be exacerbated by vortex creep and thermally activated flux flow [39–42]. Dynamics of vortices interacting with ADs and BADs is also expected to be quite different, hence dissipation involved, corresponding electric field criteria, and respective measurement type can respond differently to samples having ADs and BADs. Finally, slightly differing directions of the Lorentz forces with respect to some AD shapes may be considered. *Trans* measurements induce a Lorentz force perpendicular to either the top or bottom of each shape. On the other hand, the circulating current around the entire square film during *mag* measurements directs the vortices toward the center. In a regular triangular array like that seen in figure 1, vortices would experience a Lorentz force orientated at every point around the shape. All these effects together potentially can cause a notable difference between the two measurement types.

Both measurements types are restricted in the temperature range that they can measure (*mag* measurements need a high signal, therefore lower temperature, the *trans* experimental set-up is limited to ~100 mA to avoid excessive heating, thus require to be close to T_c). Due to this, the comparison temperatures are 0.87 T_c (77 K) for magnetic and 0.97 T_c for transport. Further differences are expected between these temperature ranges, however, a qualitative comparison may prove being useful. *Mag* samples were prepared on 5 × 5 mm^2 substrates. This was reduced to 3 × 3 mm^2 in the center to remove any edge effects, with the patterns in regular triangle arrays like that shown in figure 1 throughout the entire film. The width of the magnetization loops is determined by $\Delta M(B_a, T) = |M^+| + |M^-|$, and using the critical state model $J_c(B_a, T) = 3\Delta M/w$, where w_p is the length of one side of the square sample [37].

The ΔJ_c between the respective measurement types correlate very strongly in both magnitude and shape for 3 μm patterns (figure 4(b)), but not for the 2 μm patterns (figure 4(a)) with the ΔJ_c being approximately the same between *trans* and *mag* measurements only above ~0.05 T. Aside from a slight change in magnitude in figure 4(b), the only apparent difference is the large separation in ΔJ_c between the patterns for the *mag* measurements. The *trans* measurements on the other hand show a fairly close grouping in ΔJ_c across all B_a.

The circular hole 3 μm sample in figure 4(b) degrades the most upon magnetic measurements even though they do not have the largest volume removed (2.35 μm^3 compared to 2.40 μm^3 of a square). This suggests that there is a AD shape dependence, more than just due to AD volume removed.

One shape dependence explanation may be due to triangle and square ADs both having straight edges, which might present more of a pinning barrier for the vortex to overcome compared to circular ADs. Circle hole circumferences would always allow a tangential component of the Lorentz force to exists allowing vortices to slip around easier regardless of the current path upon magnetic or transport measurements. This would mean the circles would be

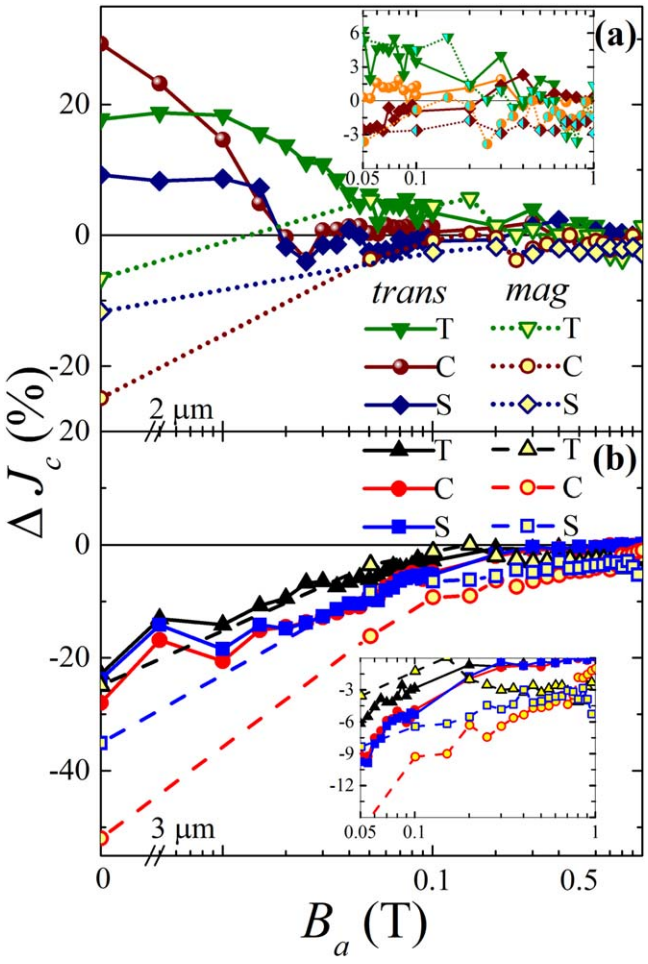

Figure 4. Comparison of ΔJ_c for (a) 2 μm and (b) 3 μm patterns between transport (*trans*) and magnetic (*mag*) measurements. Transport measurements taken at 86 K (0.97 T_c) and magnetic measurements at 77 K (0.87 T_c). Inset shows the corresponding high field (>0.05 T) data.

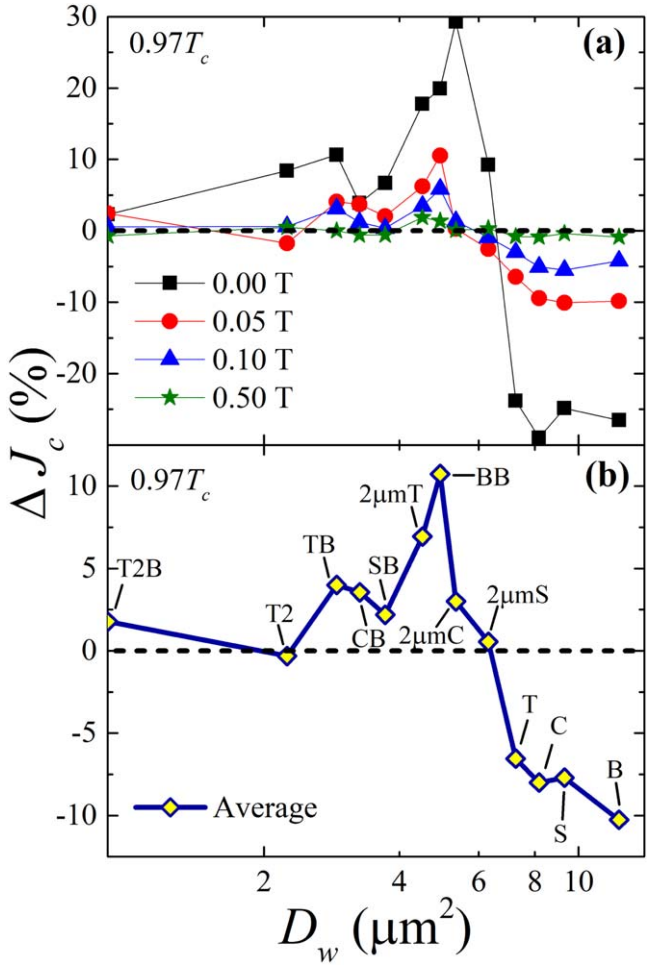

Figure 5. (a) The J_c difference as a function of the AD etched wall area for several applied magnetic fields. (b) The $\Delta J_c(D_w)$ dependence averaged over all the applied field values displayed in (a). The AD pattern types marked in (b) for each symbol correspond to those plotted in (a).

consistently worse pinning sites for all sizes. One apparent exception for 2 μm C measured by transport occurs at low field range (<0.02 T) where pinning plays less important role than current flow transparency [43, 44].

Slight discrepancies between measurement types, especially in low fields, are likely the result of these different measurement modalities discussed above in these fully perforated samples. Overall, *mag* measurements show consistently lower ΔJ_c than the *trans* measurements. This is likely due to both difference in the respective electric field criteria [37] and different measurement temperatures. However, it is currently impossible to completely disentangle these influences.

3.4. Consideration of vortex pinning by ADs and BADs

To explain the different pinning effectiveness between the different types and shapes of AD defects, ΔJ_c was plotted as a function of the etched defect wall area (D_w) calculated for each AD defect (table 1) in figure 5. The D_w value is given by a corresponding circumference multiplied by the depth of the AD or BAD defect. For instance the D_w of sample S would be 3.1 μm (optically measured length of one side) × 4 (sides) × 250 nm (etched depth) ×3 (ADs) = 9.30 μm^2, whereas the D_w of sample SB would be 3.1 μm ×4 ×100 nm ×3 = 3.72 μm^2. The junction between the etched and non-etched regions being the area of additional nano-wall pinning [34]. The obtained values for D_w are given in table 1 in order of increasing D_w. In figure 5(a), the $\Delta J_c(D_w)$ is shown at different B_a values, which displays a similar trend at all the field values with the magnitude of the ΔJ_c suppressed towards 0% at higher fields.

As expected, removing a very small volume of the superconductor (T2B) has least enhancing effect on the J_c in the superconductor compared to the corresponding plain film. On the contrary, removing relatively large volumes (all fully perforated 3 μm patterns and 5 μm B) causes a large J_c degradation relative to a plain film rather than enhancement. T2 has fully perforated AD pattern, however the full perforation is counterbalanced by a relatively small number of ADs in this pattern, so that its $\Delta J_c \simeq 0\%$.

Between T2 and 2 μm S, there appears to be the optimal region of the AD wall area with D_w being between ~2 μm^2

and $\sim 6\ \mu m^2$. This optimal AD defect wall area region appears for defects that have much greater size than the 'optimal' ($\simeq \lambda$, the magnetic field penetration depth) vortex (or/and flux) pinning [13, 31, 43, 44], which may generally complement the ξ-optimal vortex pinning.

Further emphasized in figure 5(b) are the two main factors of the defects dependence on ΔJ_c, being the pinning AD wall area, as well as, the geometrical shape of the AD defects. Within D_w of $\sim 2\ \mu m^2$ to $\sim 6\ \mu m^2$, the shape of the defect becomes the dominant factor affecting ΔJ_c. In this region, samples TB, 2 μmT and BB are more effective than CB, SB, 2 μmC and 2 μm S. This shows that J_c in the patterned samples is not entirely determined within D_w, perhaps also being dependent on the angle of this defect wall to Lorentz force direction. In general, triangles have the highest surface area to the volume ratio, meaning that samples T and B, for instance, have the most additional pinning regions compared to the volume which has been removed of the patterns measured. This implies that removing the least amount of YBCO with already huge number of intrinsic pinning defects [2, 35, 45, 46], while adding the additional pinning AD wall area, is the main guiding principle for choosing the shape, size and type of AD patterns.

The fact that a optimal region of D_w exists should not be underestimated. The entirely different pinning mechanisms between large blind holes [28, 30], where vortices exist within the hole, and large fully perforated ADs, where vortices cannot exist inside, should be appreciated. Furthermore, the size of the individual defect of T and T2 is the same, however, with the increased vertical period of T2 the value of D_w is reduced to below 6 μm^2 and enhancement to J_c [15, 47] can occur (figure 5(a)). This is opposed to T where J_c is consistently reduced (figures 5(a), (b)).

The fact that the BADs and the ADs show approximately the same ΔJ_c (on average) as long as they are within the optimal D_w region is extremely useful when designing further defect experiments and defect patterned devices. It appears that the individual defect (shape, size and type) is less important than their entire pattern, which renders a significantly simplified path of their manufacturing for the resolution dependent fabrication equipment.

4. Conclusion

Partially and fully perforated antidots of different shapes and micron-large sizes fabricated by laser lithography and ion etching in YBCO films have been shown to significantly affect their J_c. The detrimental factor responsible for critical current enhancement of up to $\sim$30% in the patterned films compared to their as-grown counterparts is found to be the area of the circumference wall of the antidots etched. The enhancing AD wall area is found only within $\sim 2\ \mu m^2$ and $\sim 6\ \mu m^2$, which can even effectively counteract the completely removed superconducting volume within ADs. However, one of the most effective J_c enhancing patterns investigated was blind boomerangs (BB). Overall, the optimal J_c enhancing surface wall area was found independent of partial or full perforation. The enhancement effect on J_c appears less dependent on the individual hole shape, but rather on the overall pattern. However, within the optimal D_w some shape dependence occurs, indicating that the geometry of the AD circumferences effectively contribute to vortex pinning as well. Further optimization of the D_w factor incorporating shape dependence would give insights on optimal AD patterns for J_c enhancement. When designing superconducting devices it becomes clear that optimization of AD positions is important to consider depending on the modality used or device created (e.g. superconducting bridge or pick-up loops [48]).

ORCID iDs

A Jones https://orcid.org/0000-0003-0031-7537
S K H Lam https://orcid.org/0000-0003-3320-5128
A V Pan https://orcid.org/0000-0001-5313-4975

References

[1] Pan A V, Pysarenko S and Dou S X 2006 Drastic improvement of surface structure and current-carrying ability in $YBa_2Cu_3O_7$ films by introducing multilayered structure *Appl. Phys. Lett.* **88** 232506
[2] Pan A V, Pysarenko S V, Wexler D, Rubanov S and Dou S X 2007 Multilayering and Ag-doping for properties and performance enhancement in $YBa_2Cu_3O_7$ films *IEEE Trans. Appl. Supercond.* **17** 3585
[3] Llordés A *et al* 2012 Nanoscale strain-induced pair suppression as a vortex-pinning mechanism in high-temperature superconductors *Nat. Mater.* **11** 329
[4] Rouco V, Bartolomé E, Maiorov B, Palau A, Civale L, Obradors X and Puig T 2014 Vortex creep in TFA-YBCO nanocomposite films *Supercond. Sci. Technol* **27** 115008
[5] Lepeshev A A *et al* 2018 Magnetic properties and critical current of superconducting nanocomposites $(1\text{-}x)YBa_2Cu_3O_{7-\delta}+xCuO$ *J. Supercond. Nov. Magn.* **31** 3841–5
[6] Gautam B *et al* 2018 Probing the effect of interface on vortex pinning efficiency of one-dimensional $BaZrO_3$ and $BaHfO_3$ artificial pinning centers in $YBa_2Cu_3O_{7-x}$ thin films *Appl. Phys. Lett.* **113** 212602
[7] Yang C-M *et al* 2017 Effect of ZnO/TiO_2 Nanorods fabricated using the electrospinning method in Y–Ba–Cu–O single grain bulk superconductors *IEEE Trans. Appl. Supercond.* **27** 6800104
[8] Khan M Z *et al* 2018 Angular and field dependent flux pinning in artificially doped YBCO films on IBAD-MgO based template *Physica* C **555** 15
[9] Horide T *et al* 2018 Geometric and compositional factors on critical current density in $YBa_2Cu_3O_{7-\delta}$ films containing nanorods *Supercond. Sci. Technol.* **31** 065012
[10] Suvorova E I *et al* 2014 Structure analysis of the YBCO layer in Ag/YBCO/metal oxide buffer/Hastelloy composite tape before and after 107 MeV Kr^{17+} irradiation *Acta Mater.* **75** 71–9
[11] Ohshima S, Takanashi N, Saito A, Nakajima K and Nagayama T 2018 Effect of Si-Ion irradiation on microwave surface resistance in $YBa_2Cu_3O_y$ thin films in magnetic fields *IEEE Trans. Appl. Supercond.* **28** 7501204

[12] Kwon J-H *et al* 2018 Extended electronic structure inhomogeneity created by double chain layer defects surrounding columnar tracks in heavy-ion irradiated $YBa_2Cu_3O_{7-\delta}$ films containing nanorods *Supercond. Sci. Technol* **31** 105006

[13] Moshchalkov V V, Baert M, Metlushko V V, Rosseel E, Van Bael M J, Temst K, Bruynseraede Y and Jonckheere R 1998 Pinning by an antidot lattice: The problem of the optimum antidot size *Phys. Rev.* B **57** 3615

[14] Baert M, Metlushko V V, Jonckheere R, Moshchalkov V V and Bruynseraede Y 1995 Composite flux-line lattices stabilized in superconducting films by a regular array of artificial defects *Phys. Rev. Lett.* **74** 3269

[15] George J *et al* 2017 Tunable pinning effects produced by non-uniform antidot arrays in YBCO thin films *Ann. Phys.* **529** 1600283

[16] Silhanek A V, Gillijns W, Moshchalkov V V, Metlushko V V, Gozzini F, Ilic B, Uhlig W C and Unguris J 2007 Manipulation of the vortex motion in nanostructured ferromagnetic/superconductor hybrids *Appl. Phys. Lett.* **90** 182501

[17] Wördenweber R, Dymashevski P and Misko V R 2004 Guidance of vortices and the vortex ratchet effect in high-T_c superconducting thin films obtained by arrangement of antidots *Phys. Rev.* B **69** 184504

[18] Jones A *et al* 2018 Changing the critical current density and magnetic properties of $YBa_2Cu_3O_7$by using large antidots *IEEE Trans. Appl. Supercond.* **28** 2808439

[19] Palau A, Monton C, Rouco V, Obradors X and Puig T 2012 Guided vortex motion in $YBa_2Cu_3O_7$ thin films with collective ratchet pinning potentials *Phys. Rev.* B **85** 012502

[20] Ortiz W A *et al* 2006 Vortex matter in a thin film of YBCO with columnar indentations-very small and moderate field regimes *Physica* C **437–438** 254

[21] VestgÅrden J I, Yurchenko V V, Wördenweber R and Johansen T H 2012 Mechanism for flux guidance by micrometric antidot arrays in superconducting films *Phys. Rev.* B **85** 014516

[22] Xue C *et al* 2018 Stability of degenerate vortex states and multi-quanta confinement effects in a nanostructured superconductor with Kagome lattice of elongated antidots *New J. Phys.* **20** 093030

[23] Selders P, Castellanos A, Vaupel M and Wördenweber R 1997 Observation of and noise reduction by vortex lattice matching in $YBa_2Cu_3O_7$ thin films and rf SQUIDs with regular arrays of antidots *App. Supercond* **5** 269–76

[24] Keil S *et al* 2018 Imaging of vortices and $1/f$ noise sources in YBCO dc SQUIDs using low-temperature scanning electron microscopy *IEEE Trans. Appl. Supercond.* **9** 2961–6

[25] Selders P and Wördenweber R 2000 Low-frequency noise reduction in $YBa_2Cu_3O_{7-\delta}$ superconducting quantum interference devices by antidots *App. Phys. Lett.* **76** 3277

[26] Tseng A A, Chen K, Chen C D and Ma K J 2003 Electron beam lithography in nanoscale fabrication: recent development *IEEE Trans. Electron. Packag. Manuf.* **26** 141–9

[27] Rouco V, Palau A, Monton C, Del-Valle N, Navau C, Sanchez A, Obradors X and Puig T 2015 Geometrically controlled ratchet effect with collective vortex motion *New J. Phys.* **17** 073022

[28] Jones A, Lam S K H, Du J, Rubanov S and Pan A V 2019 modification of pinning in $YBa_2Cu_3O_7$ thin films by substrate annealing *IEEE Trans. Appl. Supercond.* **29** 7200205

[29] Golovchanskiy I A, Pan A V, Fedoseev S A and Higgins M 2014 Significant tunability of thin film functionalities enabled by manipulating magnetic and structural nano-domains *Appl. Surf. Sci.* **311** 549

[30] Jones A, Lam S K H, Du J, Rubanov S and Pan A V 2018 Enhancing the critical current of $YBa_2Cu_3O_7$ thin films by substrate nanoengineering *J. Appl. Phys.* **124** 233905

[31] Takezawa N and Fukushima K 1997 Optimal size of an insulating inclusion acting as a pinning center for magnetic flux in superconductors: calculation of pinning force *Physica* C **290** 31–7

[32] Gheorghe D G *et al* 2006 Anisotropic avalanches and flux penetration in patterned superconductors *Physica* C **437–438** 69–72

[33] Khokhlov V A, Kosse A I, Kuzovlev Yu E, Levchenko G G, Medvedev Yu V, Yu Prokhorov A, Mikheenko P, Chakalov R and Muirhead C M 2004 Surface pinning as origin of high critical current in superconducting films *Supercond. Sci. Technol* **17** S520

[34] Palau A *et al* 2014 Nanowall pinning for enhanced pinning force in YBCO films with nanofabricated structures *Physica* C **506** 178–83

[35] Pan V M and Pan A V 2001 Vortex matter in superconductors *Low Temp. Phys.* **27** 732
Pan V M and Pan A V 2001 *Fiz. Niz. Temp.* **27** 991 (Rus.)

[36] Shantsev D V, Koblischka M R, Galperin Y M, Johansen T H, Nalevka P and Jirsa M 1999 Central peak position in magnetization loops of High-T_c superconductors *Phys. Rev. Lett.* **82** 2947

[37] Pan A V, Golovchanskiy I A and Fedoseev S A 2013 Critical current density: measurements versus reality *Europhys. Lett.* **103** 17006

[38] Golovchanskiy I A, Pan A V, Shcherbakova O V and Fedoseev S A 2013 Rectifying differences in transport, dynamic, and quasi-equilibrium measurements of critical current density *J. Appl. Phys.* **114** 163910

[39] Anderson P W and Kim Y B 1964 Hard superconductivity: theory of the motion of abrikosov flux lines *Rev. Mod. Phys.* **36** 39–43

[40] Yeshurun Y, Malozemoff A P and Shaulov A 1996 Magnetic relaxation in high-temperature superconductors *Rev. Mod. Phys.* **68** 911–49

[41] Pan A V, Ciovacco F, Esquinazi P and Lorenz M 1999 Depinning of a driven vortex lattice in high-T_c films *Phys. Rev.* B **60** 4293

[42] Pan A V and Esquinazi P 2000 The Labusch parameter of a driven flux line lattice in $YBa_2Cu_3O_7$ superconducting films *Eur. Phys. J.* B **17** 405

[43] Pan A V, Zhao Y, Ionescu M, Dou S X, Komashko V A, Flis V S and Pan V M 2004 Thermally activated depinning of individual vortices in $YBa_2Cu_3O_7$ superconducting films *Physica* C **407** 10

[44] Pan A V and Dou S X 2006 Comparison of small-field behavior in MgB_2, low- and high-temperature superconductors *Phys. Rev.* B **73** 052506

[45] Pan V, Cherpak Y, Komashko V, Pozigun S, Tretiatchenko C, Semenov A, Pashitskii E and Pan A V 2006 Supercurrent transport in $YBa_2C_3O_7$ epitaxial thin films in a dc magnetic field *Phys. Rev.* B **73** 054508

[46] Paturi P, Irjala M, Huhtinen H and Abrahamsen A B 2009 Modeling flux pinning in thin undoped and $BaZrO_3$-doped YBCO films *J. Appl. Phys.* **105** 023904

[47] Motta M *et al* 2013 Enhanced pinning in superconducting thin films with graded pinning landscapes *Appl. Phys. Lett.* **102** 212601

[48] Lam S K H 2017 Large voltage modulation in superconducting quantum interference devices with submicron-scale step-edge junctions *Physica* C **540** 20–5